

Article

Microstructure and Properties of Inconel 718 Coatings with Different Laser Powers on the Surface of 316L Stainless Steel Substrate

Yu Liu ^{1,2}, Lin Zhu ¹, Zeyu Li ¹, Miao Yu ¹, Yali Gao ^{1,*}  and Hui Liang ^{3,4}

¹ School of Mechanical Engineering, Northeast Electric Power University, Jilin 132012, China; yuliu@neepu.edu.cn (Y.L.); 18844229395@163.com (L.Z.); zeyuli0315@163.com (Z.L.); ssss5295@163.com (M.Y.)

² International Shipping Research Institute, Gongqing Institute of Science and Technology, Gongqing 332020, China

³ School of Marine Sciences, Sun Yat-sen University, Zhuhai 519028, China; 13029167163@163.com

⁴ Daqing Oilfield Powerlift Industry Co., Ltd., Daqing 163311, China

* Correspondence: dehuigyl@126.com

Abstract: Laser cladding is a new method to prepare coatings with good quality. Laser power is one of the main factors affecting the quality of laser cladding coatings. An appropriate laser power helps obtain a high-performance laser cladding coating. In order to obtain coatings with good quality, an experiment with different laser powers was designed in this research. Three Inconel 718 coatings with different laser powers were prepared on the surface of a 316L stainless steel substrate. And the effect of different laser powers (1400, 1600, and 1800 W) on the microstructure, phases, and element distribution of coatings (L1–L3) was investigated by SEM, EDS, XRD, and a wear and friction tester. Meanwhile, the microhardness and friction and wear properties of different coatings were analyzed. The results show that the coatings' phases were the same and composed of γ -(Fe, Ni) solid solution, Ni_3Nb , $(\text{Nb}_{0.03}\text{Ti}_{0.97})\text{Ni}_3$, MC_χ ($M = \text{Cr, Nb, Mo}$), and so on. The background zones in the L1–L3 coatings were mainly the Fe and Ni elements. The irregular blocks in the coating were rich in Cr, Mo, and Nb, which formed the MC_χ ($M = \text{Cr, Nb, Mo}$) phase. When laser powers were 1400, 1600, and 1800 W, the average microhardness of the three coatings was 685.6, 604.6, and 551.9 $\text{HV}_{0.2}$, respectively. The L1 coating had the maximum microhardness, 707.5 $\text{HV}_{0.2}$, because the MC_χ ($M = \text{Cr, Nb, Mo}$)-reinforced phase appeared on the upper part of the coating. The wear rates were 3.65×10^{-5} , 2.97×10^{-5} , and $6.98 \times 10^{-5} \text{ mm}^3 \cdot \text{n}^{-1} \cdot \text{m}^{-1}$. The wear mechanism of the three coatings was abrasive wear and adhesive wear. When the laser power was 1600 W, the coating had the minimum wear rate, which exhibited the best wear resistance. When the laser power was 1600 W, the upper part of the coating to the bonding zone was mainly composed of equiaxed crystals, dendrites, cellular crystals, columnar crystals, and planar crystals. The fine crystals and compounds caused a decrease in wear volume, and they had the most optimal wear resistance.



Citation: Liu, Y.; Zhu, L.; Li, Z.; Yu, M.; Gao, Y.; Liang, H. Microstructure and Properties of Inconel 718 Coatings with Different Laser Powers on the Surface of 316L Stainless Steel Substrate. *Coatings* **2023**, *13*, 1947. <https://doi.org/10.3390/coatings13111947>

Academic Editor: Antonio Ancona

Received: 22 October 2023

Revised: 10 November 2023

Accepted: 13 November 2023

Published: 15 November 2023

Keywords: laser cladding; laser power; Inconel 718; microhardness; friction and wear



Copyright: © 2023 by the authors. Licensee MDPI, Basel, Switzerland. This article is an open access article distributed under the terms and conditions of the Creative Commons Attribution (CC BY) license (<https://creativecommons.org/licenses/by/4.0/>).

1. Introduction

The 316L stainless steel is a chromium–nickel austenitic stainless steel with low carbon content, and has excellent oxidation resistance, corrosion resistance, and high-temperature resistance. Therefore, it is widely used in the fields of medical devices, and navigation, petrochemical, aviation, and automobile manufacturing [1–3]. But 316L stainless steel has a single-phase austenite structure. Its hardness and wear resistance are worse than other stainless steels. As a result, 316L stainless steel parts are prone to wear failure during service [4–6], causing significant economic losses to enterprises. For example, the minor damage of engine parts for aviation equipment is very serious, but the cost of replacing these critical parts is very high. Therefore, a proper technology is needed in order to

prevent this damage. Surface modification technology can effectively strengthen and repair the parts, and improve the hardness and wear resistance, and extend the parts' service lives [7–9]. This is of great significance in industrial production and in the protection of human life and property safety.

At present, there are many surface modification technologies, such as ion implantation technology [10], thermal spraying technology [11], and laser cladding technology [12]. Ion implantation technology requires high experimental conditions and needs to be carried out under high vacuum, which is not easy to operate. Thermal spraying technology is used to atomize the sprayed material and deposit a coating on the surface of one substrate quickly, but this coating usually has some porosities, which makes the wear resistance low. Laser cladding technology uses the irradiation of a high-energy laser beam, which makes the cladding material and substrate melt together. This coating usually has a good metallurgical bonding with the substrate [13]. This has the advantage of heat concentration, a small heat-affected zone, green pollution-free, and good metallurgical bonding [14]. Compared with the other two technologies, laser cladding technology is more suitable for the surface modification of materials.

As laser cladding technology is one of the most commonly used surface modification technologies, researchers have used this technology to prepare laser cladding coatings with different compositions and improve surface properties [10,11]. The cladding material is very important to the quality of the coating. Some high-entropy alloy powders have been used to prepare coatings [15,16]. Some research has also investigated the effect of carbides on the microstructure and hardness of the cladding coating, such as TiC, WC, and VC [17,18]. At present, the most commonly used laser cladding material in actual industrial production is a self-fusible alloy powder [19]. Because the powder contains Si and B elements, which have excellent deoxidation slag-making properties, it is called a self-fusible alloy powder. According to the difference in the main element, the types of self-fusible alloy powder include Co-based alloy powder, Ni-based alloy powder, and Fe-based alloy powder, wherein Ni-based alloy powder has excellent wear resistance, corrosion resistance, and other properties. [20–23]. So, it is widely used in the field of laser cladding. The Inconel 718 alloy powder has high strength and very good toughness, and it is selected as the cladding material in this research. However, except for the cladding alloy powder, there are many parameters during the process of laser cladding, including laser power, scanning speed, spot diameter, and lap rate, which will directly affect the temperature distribution in the melt pool and the solidification rate. Therefore, the selection of suitable process parameters is a key to obtaining a coating with good quality. The research results indicate that different laser powers will prepare coatings with different qualities [24–26]. The proper laser power is helpful to obtain good microhardness and wear resistance [27–29]. The research on preparing high-performance Inconel 718 coatings with different laser powers helps improve the service life of 316L stainless steel parts.

In this research, three Inconel 718 alloy coatings with different laser powers were prepared on the surface of a 316L stainless steel substrate by laser cladding technology. The effect of different laser powers on the microstructure and properties of the coatings was studied by SEM, EDS, XRD, and a wear and friction tester. The research results provide a theoretical basis to prepare good quality coatings on the surface of 316L stainless steel substrate during the process of laser cladding.

2. Experimental Materials and Methods

2.1. Experimental Materials

The 316L stainless steel was used as substrate. Its chemical composition is shown in Table 1. The chemical composition was provided by Wuxi Zhonggong Metal Material Co., Ltd. The mass fractions of the Cr and Ni elements are about 16.0–18.5 and 10.0%–14.0%, respectively. The mass fraction of the Mo element is about 2.0%–3.0%. The size of the 316L substrate was 50 × 30 × 10 mm. First, 316L substrate was polished to remove oxide layer on the surface, and then wiped with anhydrous ethanol.

Table 1. Chemical composition of 316L stainless steel (Mass fraction, wt.%).

Component	Fe	C	Mn	Ni	Si	Mo	Cr
Mass fraction	Bal	≤0.08	≤2.0	10.0–14.0	≤1.00	2.0–3.0	16.0–18.5

The cladding powder material was Inconel 718. And its chemical composition is shown in Table 2. The chemical composition was provided by Nangong Xindun Alloy Welding Material Spraying Co., Ltd. The mass fractions of the Fe, Co, and Si elements are 14.2, 1.0, and 0.4, respectively. The mass fractions of Cr, Nb, and Mo are 17.0–21.0, 4.8–5.5, and 2.8–3.3, respectively. In order to prevent the presence of moisture, the treatment of drying this Inconel 718 alloy powder was used. In order to place the cladding powder, a hollow polypropylene plate was put on the surface of 316L stainless steel. So, this hollow region would be filled with Inconel 718 alloy powder with a thickness of 1 mm.

Table 2. Chemical composition of Inconel 718 alloy powder (Mass fraction, wt.%).

Component	Ni	Si	Mo	Cr	Co	Ti	Nb	Fe
Mass fraction	Bal	0.4	2.8–3.3	17.0–21.0	1.0	0.7–1.2	4.8–5.5	14.2

2.2. Experimental Design

The laser energy directly affects cladding quality during the process of laser cladding. The value of input energy is proportional to the molten pool's temperature and inversely proportional to the molten pool's cooling rate. If the input energy is large, it will lead to overheating or even burning of substrate. Otherwise, if the input energy is small, it will lead to the formation of poor metallurgical bonding. When the laser power is stable, this laser cladding process can be regarded as an energy source moving along with a preset scanning path. At this time, the temperature distribution in the molten pool is shown in Equation (1) [30]:

$$T(t, r) = 2P \left\{ \frac{c\rho}{(4\pi\lambda t)^3} \right\}^{1/2} \exp\left(-\frac{c\rho r^2}{4\lambda t}\right) \quad (1)$$

wherein P is laser power, W ; r is the distance between the energy source and test point, m ; c is the specific heat capacity, $J/(kg \cdot K)$; λ is the thermal conductivity of material, $W/(m \cdot K)$; ρ is density, $kg \cdot m^{-3}$.

The cooling rate v_c in the molten pool can be expressed by Equation (2) [30]:

$$v_c = 4\pi\lambda T_b^2 v / p \quad (2)$$

wherein T_b is the temperature of test point, K ; v is the laser scanning speed, $mm \cdot s^{-1}$. It can be seen from Equation (2) that the cooling rate in the molten pool is inversely proportional to the laser power and proportional to the scanning speed. The increase in laser power can decrease the cooling rate of molten pool.

The process parameters of laser cladding are included in Table 3. The values of laser power are 1400, 1600, and 1800 W, respectively. The scanning speed is 2 mm/s. The spot diameter and overlap rate are 3 mm and 30%, respectively.

Table 3. Parameters of laser cladding process.

NO.	Laser Power (W)	Scanning Speed (mm/s)	Spot Diameter (mm)	Overlap Rate
L1	1400	2	3	30%
L2	1600	2	3	30%
L3	1800	2	3	30%

2.3. Experimental Methods

A CO₂ laser (DL-HL-T2000, Shenyang DALU Laser Technology Co., Ltd., Shenyang, China) was used with a mixed gas ratio of (CO₂:N₂:Ar = 0.048:3.7:0.31) during the process of laser cladding. The wavelength of laser is ten microns. Three laser cladding coatings were cut into small pieces with the size of 10 × 10 × 10 mm. The specimens were polished and corroded with aqua regia (HCl:HNO₃ = 3:1).

The scanning electron microscope (TESCAN MIRA, TESCAN, Brno, Czech Republic) was used to observe the micro-morphology of the coating at different positions. The elemental distribution was analyzed by energy dispersive spectrometer (TESCAN MIRA, TESCAN, Brno, Czech Republic). The phases were detected by TD-3500 X-ray diffractometer (Dandong Tongda Science and Technology Co., Ltd., Dandong, China). The microhardness of laser cladding layer was tested by HXD-1000TMC/LCD hardness tester (HXD-1000TMC/LCD, Shanghai Optical Instrument Co., Ltd., Shanghai, China). The load was 200 gf and loading time was 15 s. The friction and wear experiment was conducted by MGW-02 high-speed reciprocating fatigue friction and wear testing machine (Jinan Yihua Tribology Testing Technology Co., Ltd., Jinan, China). The material of grinding ball was GCr15. The frequency and loading load were 2 Hz and 10 N, respectively. The friction mode was dry sliding friction of non-lubricated plane-spherical surface.

3. Results and Discussion

3.1. Phases

Figure 1 shows the XRD patterns of the Inconel 718 cladding coatings with different laser powers. It can be seen that the phases of the L1–L3 coatings were all composed of γ -(Fe, Ni) solid solution (JCPDS: 03-065-5131), Ni₃Nb (JCPDS: 00-049-1427), (Nb_{0.03}Ti_{0.97})Ni₃ (JCPDS: 00-023-1275), MC_x (M = Cr, Nb, Mo) (JCPDS: 00-014-0519, JCPDS: 00-006-0546, JCPDS: 00-015-0147), and so on. The research results indicated that the phase composition of the three coatings was basically the same, even if the laser powers were different. When the diffraction peak angle was about 43°, the diffraction peak intensity of γ -(Fe, Ni) solid solution was higher in the coating, because the element Fe entered into the coating from the substrate and formed an infinitely miscible γ -(Fe, Ni) solid solution with the Ni element. When the diffraction peak angle was about 50°, the diffraction peak intensity of γ -(Fe, Ni) solid solution phase in the L1–L3 coatings gradually increased with the increase in laser power because the liquid metal's temperature in the molten pool increased along with an increase in laser power. The cooling rate was small. The crystal had sufficient time to grow, which resulted in an increase in the diffraction peak intensity of crystal plane orientation.

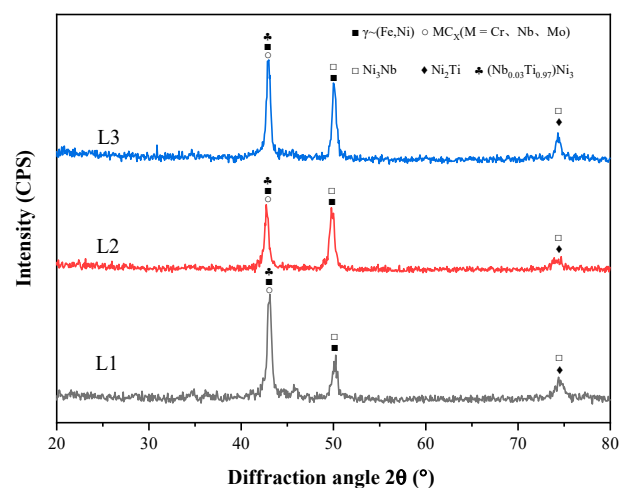


Figure 1. XRD pattern of Inconel 718 cladding coating with different laser powers.

3.2. Microstructure

Figure 2 shows the microstructure of the Inconel 718 cladding coatings with different laser powers. In Figure 2(a1), when the laser power is 1400 W, there is a clear interface between the 316L steel substrate and L1 coating. The coating near the bonding zone is mainly composed of planar crystals. In Figure 2(a2), the middle of the L1 coating is mainly composed of cellular crystals and compounds. In the middle of the coating, there are more compounds than in the bottom zone. In Figure 2(a3), the upper part of the L1 coating is mainly composed of fine network structures and coarse compounds. In Figure 2(b1), when the laser power is 1600 W, we can observe that some coarse cellular crystals and columnar crystals formed near the bonding zone of the L2 coating and grew along in the direction perpendicular to the interface of the bonding zone. The reason was that the grain growth had the principle of preferred orientation, which was more conducive to the export of heat in the direction perpendicular to the interface of the bonding zone. In Figure 2(b2), the middle of the L2 coating is mainly composed of some dendrites and compounds. But compared with the L1 coating, the crystals and compounds are finer, which is helpful to produce good properties. In Figure 2(b3), we can observe that a small amount of equiaxed crystals was generated in the upper part of the L2 coating because the higher cooling rate in the upper part of the molten pool restricts the growth of crystals. In Figure 2(c1), when the laser power is 1800 W, the bonding zone of the L3 coating is consistent with that of the L2 coating. In Figure 2(c2), we can observe that a large block structure was precipitated in the middle of the L3 coating. When the laser power was higher, there was more energy and time to help the crystals grow, which caused the structure to be coarser.

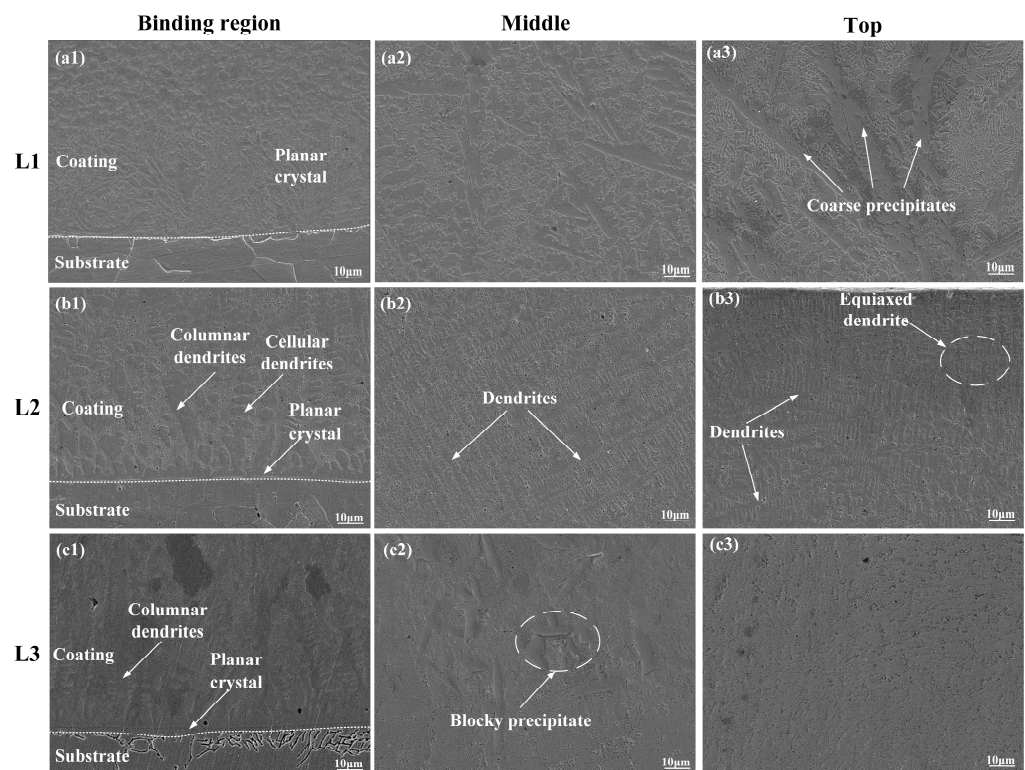


Figure 2. Microstructure of Inconel 718 cladding coatings with different laser powers.

Figure 3 shows a schematic of the L1–L3 coatings' microstructures with different laser powers. Along with the increase in laser powers, the compounds became small. When the laser power was 1600 W, there were a lot of dendrites and columnar crystals. They had a fine and uniform microstructure. When the laser power was 1800 W, the input energy of the molten pool was large, which caused some large compounds and columnar crystals.

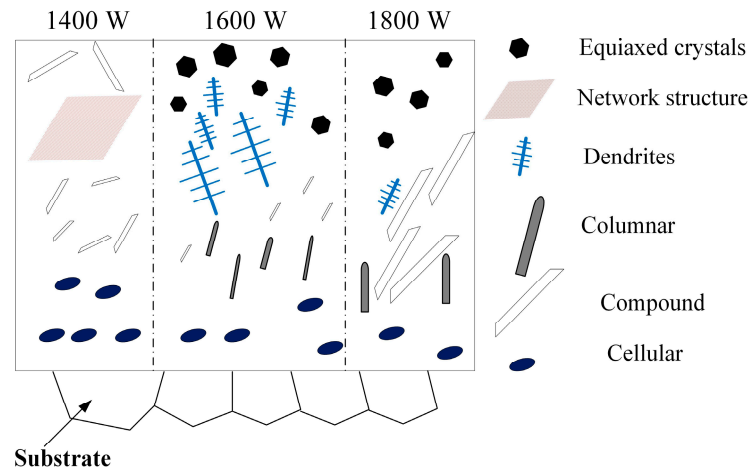


Figure 3. A schematic of L1–L3 coatings’ microstructures.

3.3. Element Distribution

Figure 4 shows the SEM of the Inconel 718 cladding coatings with different laser powers. In order to investigate the element composition, two points were selected from each coating. One point was selected from the background zone. The other point was selected from the compound. Then, two selected points from the L1–L3 coatings were analyzed with EDS.

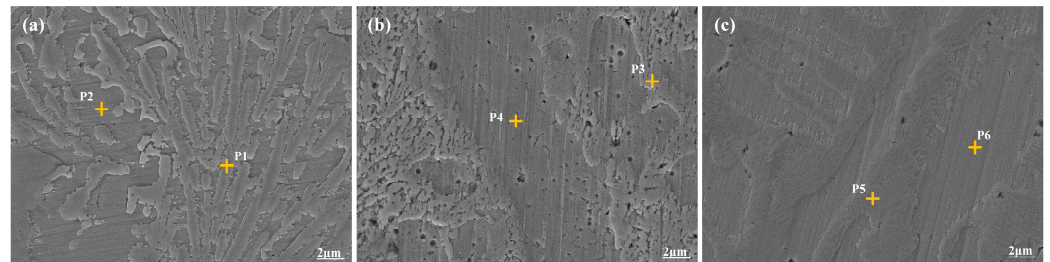


Figure 4. SEM of the bonding zone of Inconel 718 cladding coatings: (a) L1; (b) L2; (c) L3.

Table 4 includes the elemental composition of the Inconel 718 cladding coatings with different laser powers. The points of P2, P4, and P6 represent the background zone of the L1–L3 coating. From the elemental distribution in Table 4, the background zones in the L1–L3 coatings were mainly the Fe and Ni elements. With the increase in laser power, the content of Fe and Ni had an upward trend, because the molten pool had more energy along with the increase in laser power. This would increase the amount of Fe in the molten pool, and more Fe and Ni elements formed $\gamma\text{-(Fe, Ni)}$ solid solution. From the elemental distribution at the P1, P3, and P5 points, it can be seen that Cr, Mo, and Nb were enriched at the grain boundary and formed the MC_X ($M = \text{Cr, Nb, Mo}$) phase.

Table 4. Elemental composition of Inconel 718 cladding coatings with different laser power (wt.%).

Element	P1	P2	P3	P4	P5	P6
Ni	38.29	40.31	33.87	42.48	29.11	44.42
Fe	31.58	37.41	37.18	39.84	38.05	41.31
Cr	16.72	14.69	21.48	13.62	25.22	10.06
Mo	6.53	0.65	3.52	1.31	4.34	1.24
Nb	1.60	0.09	1.08	0.25	0.87	0.17
Si	4.64	6.30	2.19	2.04	1.83	2.23
Mn	0.53	0.55	0.67	0.46	0.58	1.04

The coarse compounds in the upper part of the L1 coating were scanned and investigated by the line scan of EDS. The results are shown in Figure 5. From the fluctuation of Cr, Mo, and Nb, they were enriched in the long strip structure, which formed the MC_X ($M = Cr, Nb, Mo$) phase in accordance with the XRD pattern analysis.

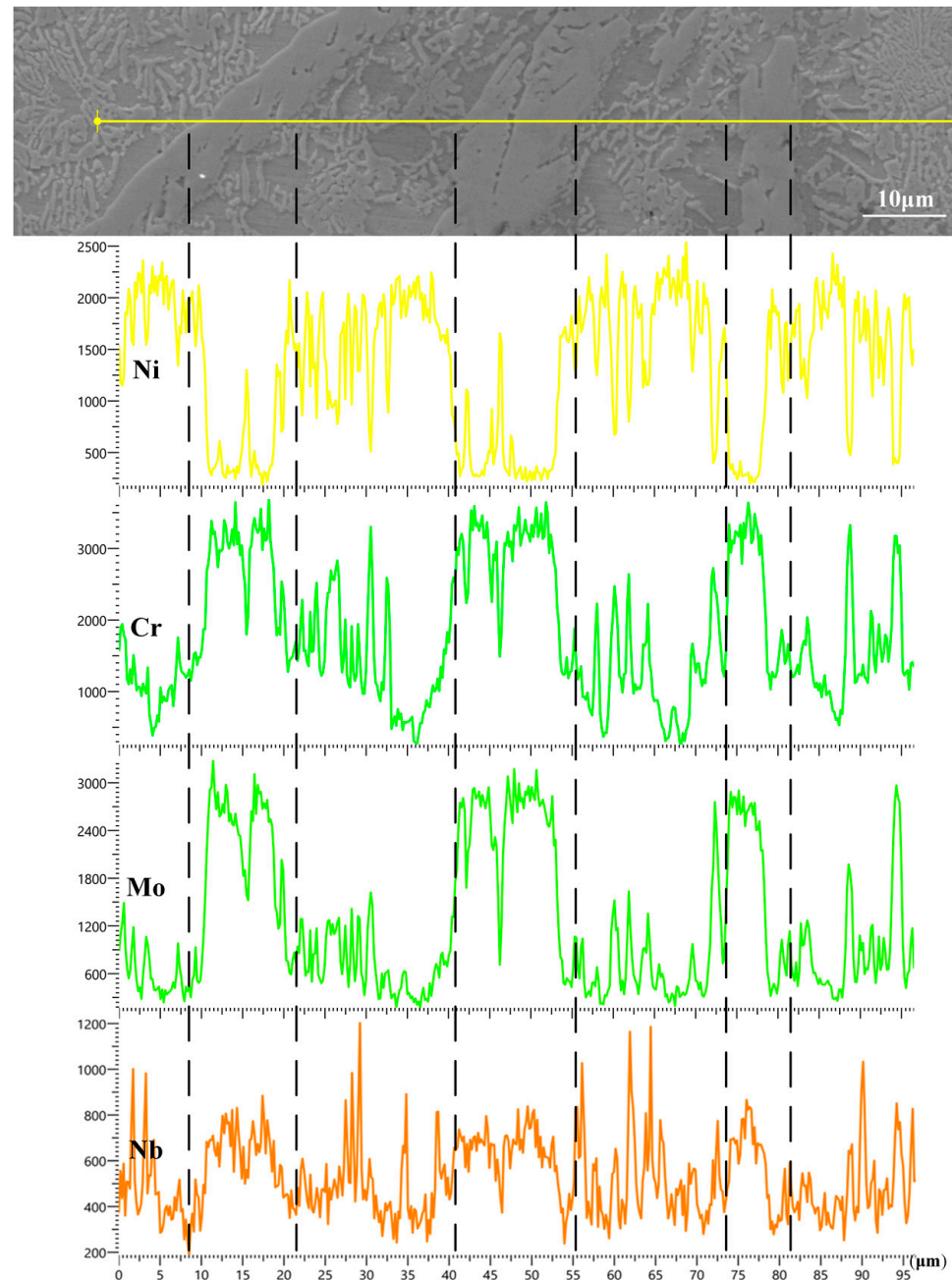


Figure 5. EDS line scan of coarse compounds in L1 coating.

Figure 6 shows the SEM image and elemental distribution of dendrites in the L2 coating. In Figure 6b,c, the dendrite arms and background zone mainly contain some Fe and Ni elements, which are the phase of the γ -(Fe, Ni) solid solution. As can be seen from Figure 6e–g, there are also some Cr, Mo, and Nb elements distributed near the grain boundaries.

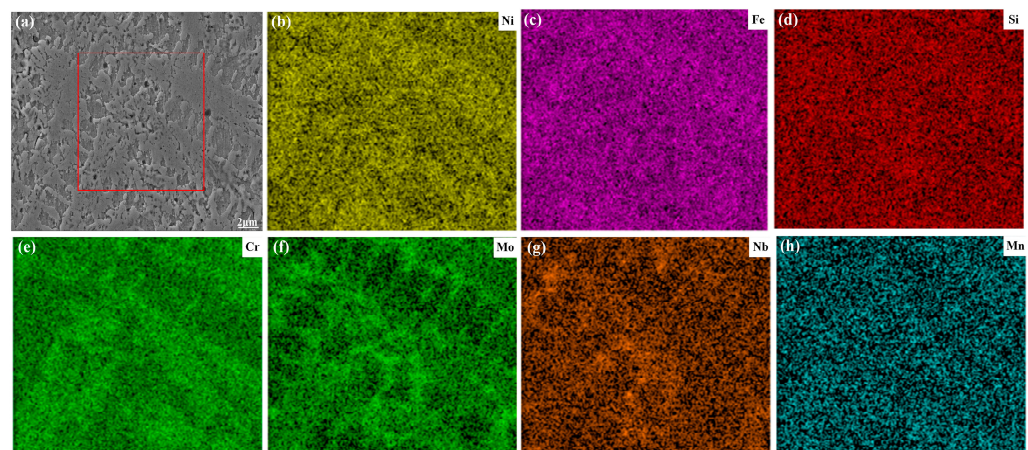


Figure 6. SEM image (a) and elemental distribution of Ni (b), Fe (c), Si (d), Cr (e), Mo (f), Nb (g), Mn (h) of dendrites in L2 coating.

Figure 7 shows the SEM image and elemental distribution of irregular blocks in the L3 cladding coating. In Figure 7b,c, the surrounding background zone mainly contain Fe and Ni elements, which is the phase of the γ -(Fe, Ni) solid solution. In Figure 7e–g, the irregular blocks in the L3 coating are rich in Cr, Mo, and Nb, which is the MC_x ($M = Cr, Nb, Mo$) phase. From the analysis of the area scan of EDS about the Cr, Mo, and Nb elements, those three elements were more obvious, indicating that the enrichment degree of Cr, Mo, and Nb in the L3 coating was higher.

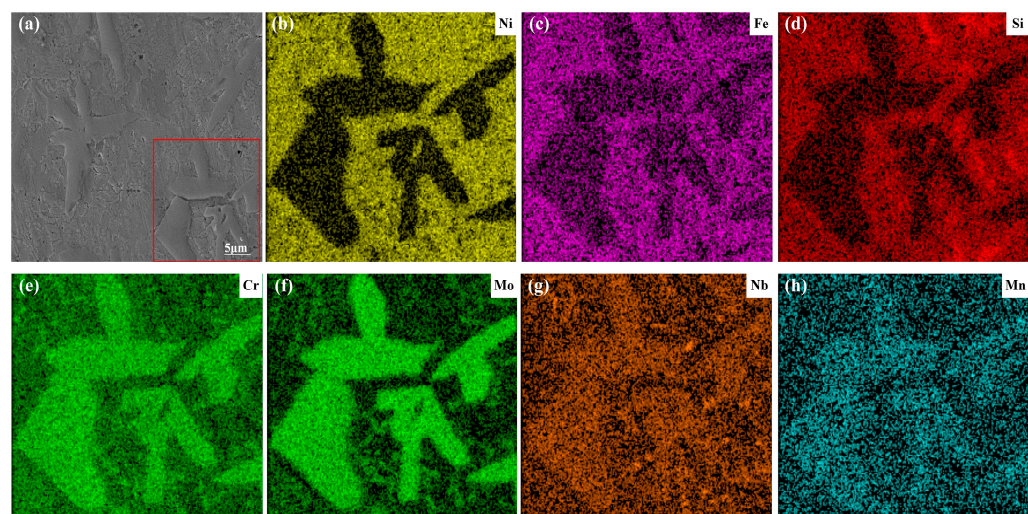


Figure 7. SEM image (a) and elemental distribution of Ni (b), Fe (c), Si (d), Cr (e), Mo (f), Nb (g), Mn (h) of irregular blocks in L3 cladding coating.

Figure 8 shows a schematic of the L1–L3 coatings' elemental distribution. The depth and width of the molten pool increased along with the increase in laser power. When the laser power was 1800 W, there were more Fe elements in the molten pool. It had a higher temperature. The Cr, Mo, and Nb elements had more time to form compounds.

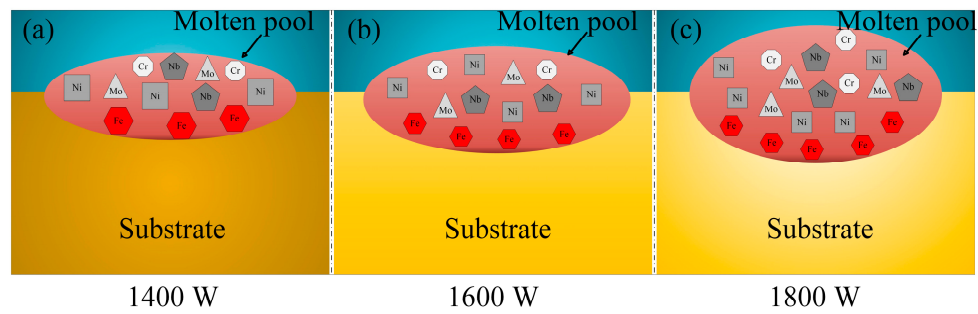


Figure 8. A schematic of L1–L3 (a–c) coatings’ elemental distribution.

3.4. Microhardness

Figure 9 shows the microhardness change in the cross section of the three coatings with different laser powers. The average microhardness values of the L1–L3 coatings were 685.6, 604.6, and 551.9 HV_{0.2} at different laser powers, respectively. The average microhardness of the L1 coating was higher than that of the other two coatings. Meanwhile, the L1 coating had the maximum microhardness, which was about 707.5 HV_{0.2}. The reason is that the MC_x (M = Cr, Nb, Mo)-reinforced phase appeared on the upper part of the L1 coating due to a low laser power, which improved the microhardness of the L1 coating. In the direction from the surface to bottom, the microhardness of the L1 coating first decreased at the distance of 0.5 mm, because its layer had a small thickness. The average microhardness of the L2 coating was slightly lower than that of the L1 coating, but the microhardness distribution of the L2 coating was more uniform. From the microstructure and elemental distribution of the L2 coating, the crystal structure was flat and had a clear boundary. The reinforced phases of MC_x (M = Cr, Nb, Mo) were tiny and evenly distributed. The microhardness of the L3 coating was lower than that of the L2 coating. With the increase in laser power, the energy in the molten pool increased. The overheated molten pool was liquid for a long time. The Fe and Ni elements increased to form more $\gamma\sim(\text{Fe}, \text{Ni})$ solid solution, which produced a lower microhardness.

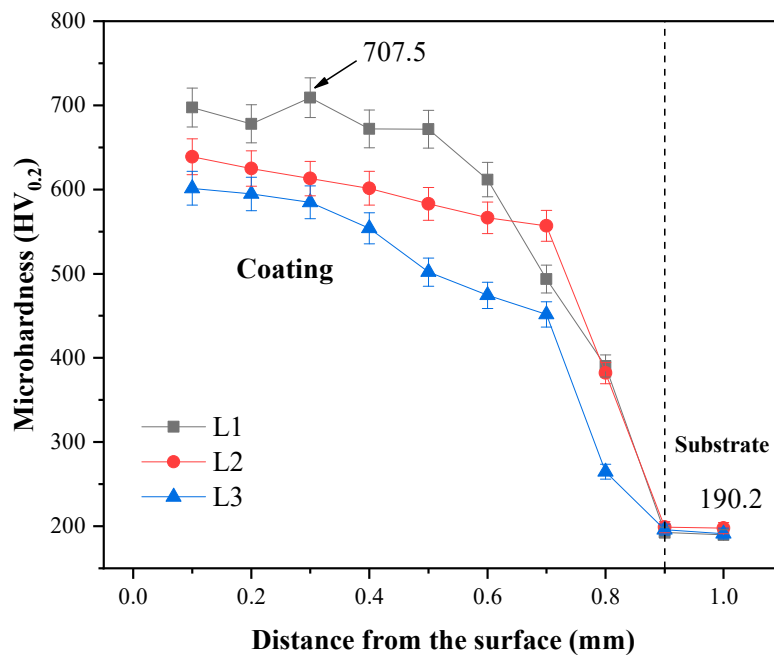


Figure 9. Microhardness of three coatings with different laser powers.

3.5. Friction and Wear

The experiments were carried out at room temperature. The wear rates of the 316L substrate and L1–L3 coatings are shown in Figure 10. It can be seen that the wear rate of the 316L substrate was $12.82 \times 10^{-5} \text{ mm}^3 \cdot \text{N}^{-1} \cdot \text{m}^{-1}$, while the wear rates of the L1–L3 coatings were 3.65×10^{-5} , 2.97×10^{-5} , and $6.98 \times 10^{-5} \text{ mm}^3 \cdot \text{N}^{-1} \cdot \text{m}^{-1}$, respectively. All three coatings had a small wear rate obviously compared to the 316L substrate. Among them, the wear rate of the L2 coating was the lowest one.

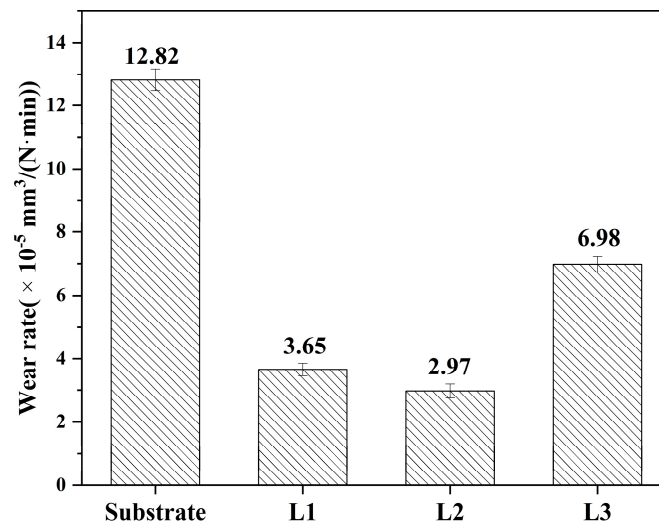


Figure 10. Wear rate of 316L substrate and L1–L3 coatings with different laser powers.

The L1 coating had the highest microhardness value, but its wear rate was not the lowest. Although there were many reinforced phases of MC_X ($M = \text{Cr}, \text{Nb}, \text{Mo}$) in the L1 coating, there were no obvious dendrites. During the process of the friction and wear experiment, plastic deformation was prone to appear due to the lack of dendrites, which resulted in a higher wear rate. However, the dendrites in the L2 coating were regular and orderly, which could resist the friction and wear better. The microstructure structure in dendrites L3 coating was relatively coarse. It made the wear rate higher and wear resistance worse.

Figure 11 shows the friction and wear morphology of dendrites 316L substrate and L1–L3 coatings with different laser powers. In Figure 11a, it can be seen that some flake spalling with a large area and debris appeared on the wear surface of the 316L substrate. In Figure 11b, the wear surface of the L1 coating has some obvious furrows and spalling pits, which demonstrated that the wear resistance was worse. In Figure 11c, the spalling pits of the L2 coating are small and shallow. Its wear morphology is relatively smooth because the microhardness and dendrites of the L2 coating were evenly distributed at this time, which only caused slight furrows and some small spalling pits. In Figure 11d, there are some deep furrows and large flake spalling on the surface of the L3 coating. The reason was that the microhardness of the L3 coating was lower. It made the wear resistance worse. The main wear mechanism of the 316L substrate was mainly adhesive wear; nevertheless, the main wear mechanism of the cladding coating with different laser powers was mainly adhesive wear and abrasive wear. The same reinforced phases produced the same wear mechanism at different laser powers. Meanwhile, it also can be seen that the L2 coating had a lower wear rate and better wear morphology. The proper laser power could obtain a good coating with better properties.

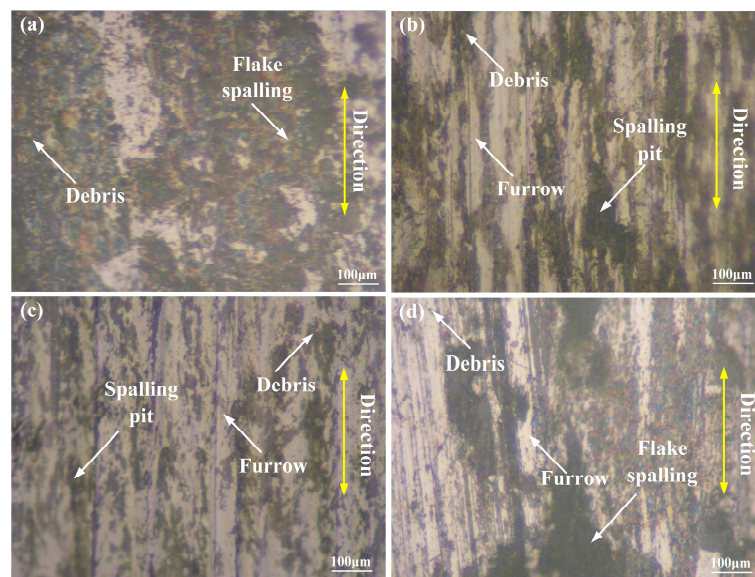


Figure 11. Friction and wear morphology of 316L substrate (a) and L1–L3 (b–d) coatings with different laser powers.

4. Conclusions

In this paper, three Inconel 718 cladding coatings were fabricated on the surface of a 316L stainless steel substrate. It is helpful to improve the property of 316L stainless steel parts. The conclusions were as follows:

- (1) All three Inconel 718 coatings with different laser powers had a good metallurgical bonding with the 316L stainless steel substrate. The phases were mainly composed of γ -(Fe, Ni) solid solution, Ni_3Nb , $(\text{Nb}_{0.03}\text{Ti}_{0.97})\text{Ni}_3$, and MC_x ($M = \text{Cr}, \text{Nb}, \text{Mo}$). The morphology of the L1–L3 coatings changed from an irregular crystal to a flat crystal along with the increase in laser power. When the laser power was 1600 W, there were some cellular crystals, columnar crystals, dendrites, and compounds.
- (2) From the EDS analysis, the background zones in the L1–L3 coatings were mainly the Fe and Ni elements. With the increase in laser power, the content of Fe and Ni had an upward trend, and they formed more γ -(Fe, Ni) solid solution. The irregular blocks in the coating were rich in Cr, Mo, and Nb, which formed the MC_x ($M = \text{Cr}, \text{Nb}, \text{Mo}$) phase. When the laser power was 1600 W, the amount of Cr, Mo, and Nb was larger, indicating that the enrichment degree of Cr, Mo, and Nb was higher in the MC_x phases of the L3 coating.
- (3) The average microhardness values of the L1–L3 coatings were 685.6, 604.6, and 551.9 $\text{HV}_{0.2}$, respectively. The L1 coating had the maximum microhardness, which was about 707.5 $\text{HV}_{0.2}$, because the MC_x ($M = \text{Cr}, \text{Nb}, \text{Mo}$)-reinforced phase appeared on the upper part of the L1 coating due to the low laser power. But the microhardness distribution of the L2 coating was more uniform. The crystals of the reinforced phase MC_x ($M = \text{Cr}, \text{Nb}, \text{Mo}$) were tiny and evenly distributed. When the laser power was 1800 W, the molten pool received more energy, and it caused the crystals to grow large.
- (4) The main wear mechanism of the 316L substrate was mainly adhesive wear; nevertheless, the main wear mechanism of the L1–L3 cladding coating with different laser powers was mainly adhesive wear and abrasive wear due to the existence of the reinforced phases. The wear rates of the L1–L3 coatings were 3.65×10^{-5} , 2.97×10^{-5} , and $6.98 \times 10^{-5} \text{ mm}^3 \cdot \text{N}^{-1} \cdot \text{m}^{-1}$, respectively. When the laser power was 1600 W, the wear rate of the L2 coating was the lowest due to the fine crystals and compounds.
- (5) The proper laser power was found to prepare a good coating with better properties on the surface of 316L stainless steel, which was 1600 W. In future work, research on different scanning speeds and different cladding materials deserves to be investigated further on the surface of 316L stainless steel.

Author Contributions: Conceptualization, Y.L., Y.G. and Z.L.; Methodology, Y.L., Y.G. and L.Z.; Data curation, Z.L. and Y.G.; Writing—original draft, Z.L., M.Y. and L.Z.; Writing—review and editing, Y.L., L.Z. and H.L.; Supervision, Y.L., M.Y. and H.L.; Funding acquisition, Y.L. All authors have read and agreed to the published version of the manuscript.

Funding: This work was supported by the Science and Technology Development of Jilin Province (20230101335JC).

Institutional Review Board Statement: Not applicable.

Informed Consent Statement: Not applicable.

Data Availability Statement: Data are contained within the article.

Conflicts of Interest: Author Hui Liang was employed by the company Daqing Oilfield Powerlift Industry Co., Ltd. The remaining authors declare that the research was conducted in the absence of any commercial or financial relationships that could be construed as a potential conflict of interest.

References

1. Ding, H.H.; Yang, T.; Wang, W.J.; Zhu, Y.; Lin, Q.; Guo, J.; Xiao, Q.; Gan, L.; Liu, Q.Y. Optimization and wear behaviors of 316L stainless steel laser cladding on rail material. *Wear* **2023**, *523*, 204830. [[CrossRef](#)]
2. Ahmed, N.; Barsoum, I.; Haidemenopoulos, G.; Al-Rub, R.A. Process parameter selection and optimization of laser powder bed fusion for 316L stainless steel: A review. *J. Manuf. Process.* **2022**, *75*, 415–434. [[CrossRef](#)]
3. Mohammadreza, D.; Hamid, R.B.R.; Abbas, S.; Mahmood, R.; Ashish, K.K.; Seeram, R.; Pradeep, L.M.; Manoranjan, M.; Ahmad, F.I.; Safian, S. Surface modification of magnesium alloys using thermal and solid-state cold spray processes: Challenges and latest progresses. *J. Magnes. Alloys* **2022**, *10*, 2025–2061.
4. Kumaradhas, P.; Sivapragash, M. Comparison of corrosion behaviour of heat treated, ZrO₂ and ZrN PVD coated AZ91D Mg alloy. *Mater. Today Proc.* **2022**, *56*, 527–532. [[CrossRef](#)]
5. Diao, Q.W.; Zou, H.B.; Ren, X.Y.; Wang, C.S.; Wang, Y.; Li, H.Y.; Sui, T.Y.; Lin, B.; Yan, S. A focused review on the tribological behavior of C/SiC composites: Present status and future prospects. *J. Eur. Ceram. Soc.* **2023**, *43*, 3875–3904. [[CrossRef](#)]
6. Parveez, B.; Kittur, M.I.; Badruddin, I.A.; Kamangar, S.; Hussien, M.; Umarfarooq, M.A. Scientific advancements in composite materials for aircraft applications: A review. *Polymers* **2022**, *14*, 5007. [[CrossRef](#)]
7. Liu, Y.; Li, Z.Y.; Li, G.H.; Tang, L. Friction and wear behavior of Ni-based alloy coatings with different amount of WC-TiC ceramic particles. *J. Mater. Sci.* **2023**, *58*, 1116–1126. [[CrossRef](#)]
8. Fedor, A.; Igor, M.; Sergey, S.; Fabio, F.; Nikita, M.; Jacobus, M.S.; Vasily, V.Z.; Igor, A.M.; Alexey, K.; Marcelo, A. Laser-induced electron dynamics and surface modification in ruthenium thin films. *Vacuum* **2023**, *212*, 112045.
9. Ayushi, T.; Swaroop, G.; Kandasubramanian, B. Electroless nickel fabrication on surface modified magnesium substrates. *Def. Technol.* **2019**, *15*, 636–644.
10. Eepsita, P.; Saurabh, P.; Kamla, R. Gold-carbon dot (Au@Cd) nanoconjugates based electrochemical sensing of cholesterol and effect of nitrogen ion implantation on sensitivity. *Biochem. Biophys. Res. Commun.* **2023**, *655*, 97–103.
11. Li, C.J.; Luo, X.T.; Yao, S.W.; Li, G.R.; Li, C.X.; Yang, G.J. The bonding formation during thermal spraying of ceramic coatings: A review. *J. Therm. Spray Technol.* **2022**, *31*, 780–817. [[CrossRef](#)]
12. Koti, D.; Powell, J.; Naestrom, H.; Voisey, K.T. Powder catchment efficiency in laser cladding (directed energy deposition). An investigation into standard laser cladding and the ABA cladding technique. *J. Laser Appl.* **2023**, *35*, 012025. [[CrossRef](#)]
13. Shi, F.K.; Zhang, Q.K.; Xu, C.; Hu, F.Q.; Yang, L.J.; Zheng, B.Z.; Song, Z.L. In-situ synthesis of NiCoCrMnFe high entropy alloy coating by laser cladding. *Opt. Laser Technol.* **2022**, *151*, 108020. [[CrossRef](#)]
14. John, M.; Kuruveri, U.B.; Menezes, P.L. Laser cladding-based surface modification of carbon steel and high-alloy steel for extreme condition applications. *Coatings* **2022**, *12*, 1444. [[CrossRef](#)]
15. Li, F.; Zheng, S.; Zhou, F. Study on Mechanical properties of AlFeCrMoNi_{1.8}Nb_{1.5} eutectic high-entropy alloy coating prepared by wide-band laser cladding. *Coatings* **2023**, *13*, 1077. [[CrossRef](#)]
16. Li, M.; Li, C.; Li, B.; Zhou, Y.; Huang, L.; Cai, A.; Cui, C.; Gao, S.; Zhang, G.; Yang, B. Comparison of Fe₃₀Co₂₀Cr₂₀Ni₂₀Mo_{3.5} high entropy alloy coatings prepared using plasma cladding, high-speed laser cladding, and deep laser cladding. *Coatings* **2023**, *13*, 1819. [[CrossRef](#)]
17. Chen, C.; Wang, J.; Ge, Y.; Zhuang, M.; Ma, Z. Microstructure and wear resistance of high-chromium cast iron with multicomponent carbide coating via laser cladding. *Coatings* **2023**, *13*, 1474. [[CrossRef](#)]
18. Mohazzab, B.F.; Jaleh, B.; Fattah-alhosseini, A.; Mahmoudi, F.; Momeni, A. Laser surface treatment of pure titanium: Microstructural analysis, wear properties, and corrosion behavior of titanium carbide coatings in Hank's physiological solution. *Surf. Interfaces* **2020**, *20*, 100597. [[CrossRef](#)]
19. Zimogliadova, T.A.; Bataev, A.A.; Lazurenko, D.V.; Bataev, I.A.; Bataev, V.A.; Golkovskii, M.G.; Saage, H.; Ogneva, T.S.; Ruktuev, A.A. Structural characterization of layers fabricated by non-vacuum electron beam cladding of Ni-Cr-Si-B self-fluxing alloy with additions of niobium and boron. *Mater. Today Commun.* **2022**, *33*, 104363. [[CrossRef](#)]

20. Jie, M.; Gao, Y.L. Study on hardness and wear resistance of laser cladding Al-Si coating. *Appl. Laser* **2015**, *35*, 629–633.
21. Shi, X.; Wen, D.; Wang, S.; Wang, G.; Zhang, M.; Li, J.; Xue, C. Investigation on friction and wear performance of laser cladding Ni-based alloy coating on brake disc. *Optik* **2021**, *242*, 167227. [[CrossRef](#)]
22. Wang, Q.; Zhai, L.L.; Zhang, L.; Zhang, J.W.; Ban, C.Y. Effect of steady magnetic field on microstructure and properties of laser cladding Ni-based alloy coating. *J. Mater. Res. Technol.* **2022**, *17*, 2145–2157. [[CrossRef](#)]
23. Gao, Z.; Ren, H.; Geng, H.; Yu, Y.; Gao, Z.; Zhang, C. Effect of CeO₂ on microstructure and wear property of laser cladding Ni-Based coatings fabricated on 35CrMoV Steel. *J. Mater. Eng. Perform.* **2022**, *31*, 9534–9543. [[CrossRef](#)]
24. Figueredo, E.W.A.; Apolinario, L.H.R.; Santos, M.V.; Silva, A.C.S.; Avila, J.A.; Lima, M.S.F.; Santos, T.F.A. Influence of laser beam power and scanning speed on the macrostructural characteristics of AISI 316L and AISI 431 stainless steel depositions produced by laser cladding process. *J. Mater. Eng. Perform.* **2021**, *30*, 3298–3312. [[CrossRef](#)]
25. Nie, M.H.; Zhang, S.; Wang, Z.Y.; Zhang, C.H.; Chen, H.T.; Chen, J. Effect of laser power on microstructure and interfacial bonding strength of laser cladding 17-4PH stainless steel coatings. *Mater. Chem. Phys.* **2022**, *275*, 125236. [[CrossRef](#)]
26. Zhang, H.; Pan, Y.J.; Zhang, Y.; Lian, G.F.; Cao, Q. Influence of laser power on the microstructure and properties of in-situ NbC/WCoB–TiC coating by laser cladding. *Mater. Chem. Phys.* **2022**, *290*, 126636. [[CrossRef](#)]
27. Hu, Z.; Li, W.; Zhao, Y. The effect of laser power on the properties of M₃B₂-type boride-based cermet coatings prepared by laser cladding synthesis. *Materials* **2020**, *13*, 1867. [[CrossRef](#)]
28. Shayanfar, P.; Daneshmanesh, H.; Janghorban, K. Parameters optimization for laser cladding of inconel 625 on ASTM A592 steel. *J. Mater. Res. Technol.* **2020**, *9*, 8258–8265. [[CrossRef](#)]
29. Huang, Y.; Hu, Y.; Zhang, M.; Mao, C.; Wang, K.; Tong, Y.; Li, K. Multi-objective optimization of process parameters in laser cladding CoCrCuFeNi high-entropy alloy coating. *J. Therm. Spray Technol.* **2022**, *31*, 1985–2000. [[CrossRef](#)]
30. Li, Z.Y. Research on laser cladding layer on the surface of the stainless steel and its properties. *Dissertation* **2023**, *17*, 130005.

Disclaimer/Publisher’s Note: The statements, opinions and data contained in all publications are solely those of the individual author(s) and contributor(s) and not of MDPI and/or the editor(s). MDPI and/or the editor(s) disclaim responsibility for any injury to people or property resulting from any ideas, methods, instructions or products referred to in the content.